Supporting Information

Ni/Fe bimetallic ions co-doped manganese dioxide cathode materials for aqueous zinc-ion batteries

Feifei Gao†, Wenchao Shi†, Bowen Jiang†, Zhenzhi Xia, Lei Zhang and Qinyou An*

State Key Laboratory of Advanced Technology for Materials Synthesis and Processing,

Wuhan University of Technology, Wuhan, 430070, China

* Correspondence: anqinyou86@whut.edu.cn
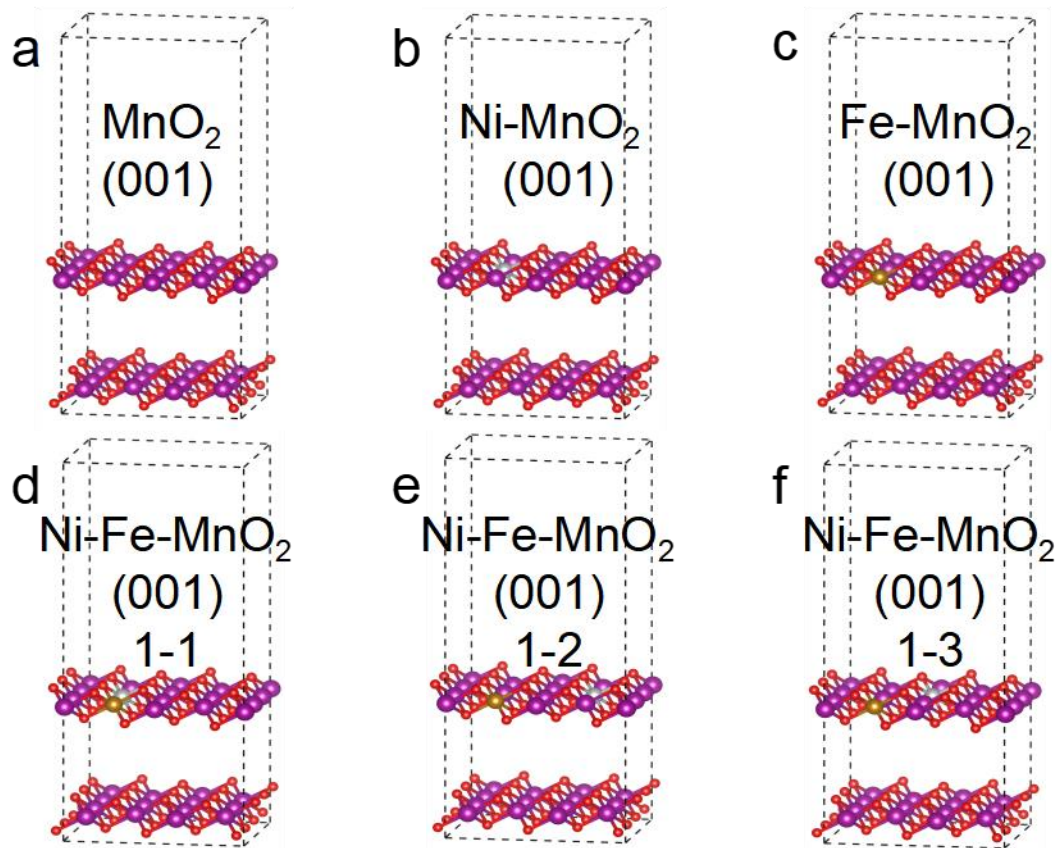
† These authors contributed equally to this work.

Figure S1. (a-f) Six structural models for the first-principles calculations: (a) MnO_2, (b) Ni-MnO_2, (c) Fe-MnO_2, (d) Ni-Fe-MnO_2 (1-1), (e) Ni-Fe-MnO_2 (1-2), (f) Ni-Fe-MnO_2 (1-3).

Table S1. The minimum formation energy for three different NFMO structural models.

Structure	Ni-Fe-MnO_2 1-1	Ni-Fe-MnO_2 1-2	Ni-Fe-MnO_2 1-3
Formation energy (eV)	4.86986	5.00333	5.81854

The structural models of different occupation positions of Fe and Ni atoms were optimized and calculated their minimum formation energy. The formula for the formation energy of the Fe-Ni-MnO$_2$ structure is defined as follows:

$$E_f = E_{TM/Slab} - \frac{E_{TM}}{N_{TM}} - E_{Slab} \tag{1}$$

Here, E_f is the formation energy of the Fe-Ni-MnO$_2$ structure. $E_{TM/Slab}$ is the total energy of transition metal doped on slab. E_{TM} is the total energy of transition metal bulk. N_{TM} is the number of transition metal ions. E_{Slab} is the total energy of pristine slab. We calculate the minimum formation energy of the Ni-Fe-MnO$_2$ (1-1), Ni-Fe-MnO$_2$ (1-2) and Ni-Fe-MnO$_2$ (1-3) structures as 4.87 eV, 5.00 eV and 5.82 eV, respectively, according to formulas (1). The minimum formation energy for three different Ni-Fe-MnO$_2$ structure models is provided in Table S1. Obviously, the formation energy of the Ni-Fe-MnO$_2$ (1-1) structure is lower than that of Ni-Fe-MnO$_2$ (1-2) and Ni-Fe-MnO$_2$ (1-3) structures, which indicates that the Ni-Fe-MnO$_2$ (1-1) structure is more stable than the Ni-Fe-MnO$_2$ (1-2) and Fe-Ni-MnO$_2$ (1-3) structures. It may be easier to synthesize the Ni-Fe-MnO$_2$ (1-1) structure in experimental conditions. Thus, the Ni-Fe-MnO$_2$ (1-1) structure is considered the most reasonable structure for theoretical calculation in this work.
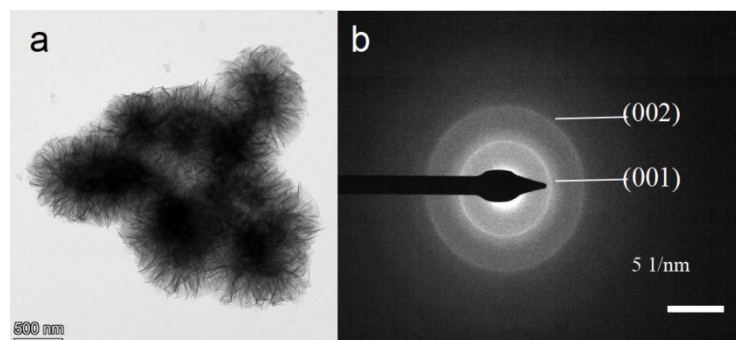
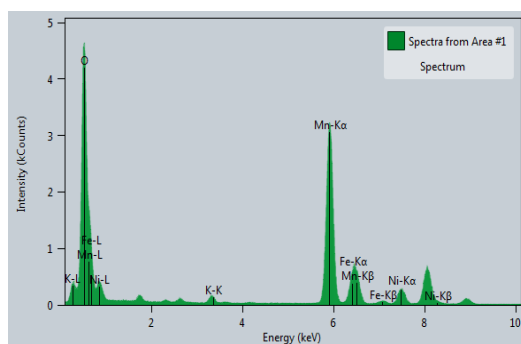**Figure S2**. (a) TEM images and (b) SAED patterns of the NFMO sample.

Figure S3. EDS analysis result for the marked area of TEM.

Table S2. Element composition analysis of NFMO.

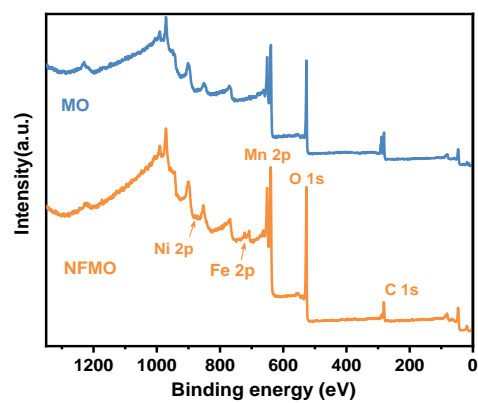| Z	Element	Family	Atomic Fraction (%)	Atomic Error(%)	Mass Fraction(%)	Mass Error (%)	Fit error (%)
8	O	K	67.79	6.84	38.05	2.55	0.48
19	K	K	0.97	0.20	1.33	0.25	0.38
25	Mn	K	25.63	4.29	49.39	7.37	0.28
26	Fe	K	3.19	0.53	6.25	0.93	0.30
28	Ni	K	2.42	0.40	4.98	0.74	0.58

Figure S4. XPS characterization of survey spectrum.

Table S3. ICP analysis of the four cathode materials (MO, NMO, FMO and NFMO).

Sample	Mn (w%)	K (w%)	Ni (w%)	Fe (w%)	Mn:Ni molar ratio	Mn:Fe molar ratio
MO	49.11365011	6.60615936	0	0	0	0
NMO	49.32362234	3.29900069	10.17830249	0	1：0.1932	0
FMO	48.86557160	3.22774565	0	9.72753283	0	1：0.1958
NFMO	47.41089504	1.87722062	4.92516906	4.63014636	1：0.0972	1：0.0961

$$2KMnO_4 \triangleq K_2MnO_4 + MnO_2 + O_2 \qquad (1)$$
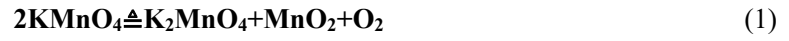
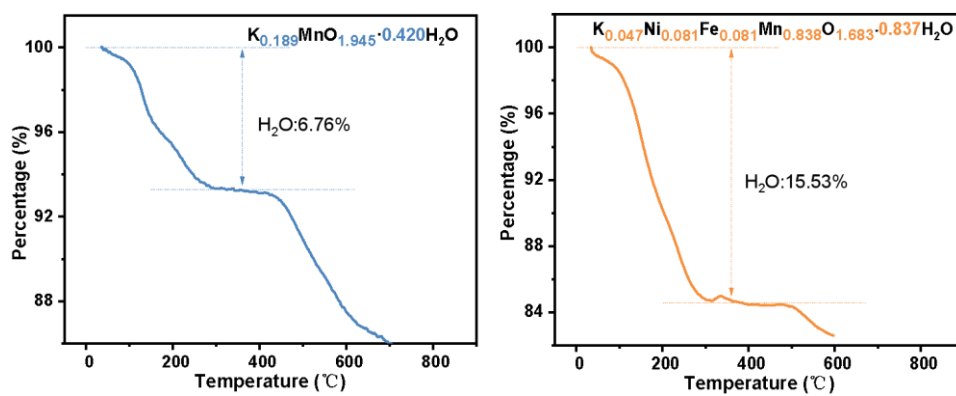The formula (1) is the reaction equation of MnO_2 preparation.

Figure S5. Exact molecular formula of δ-MnO$_2$ based on the TGA, XPS and ICP results. (a) δ-MnO$_2$ without Ni-doping: K$_{0.189}$MnO$_{1.945}$·0.420H$_2$O, (b) δ-MnO$_2$ with Ni and Fe-doping: K$_{0.047}$Ni$_{0.081}$Fe$_{0.081}$Mn$_{0.838}$O$_{1.683}$·0.837H$_2$O.
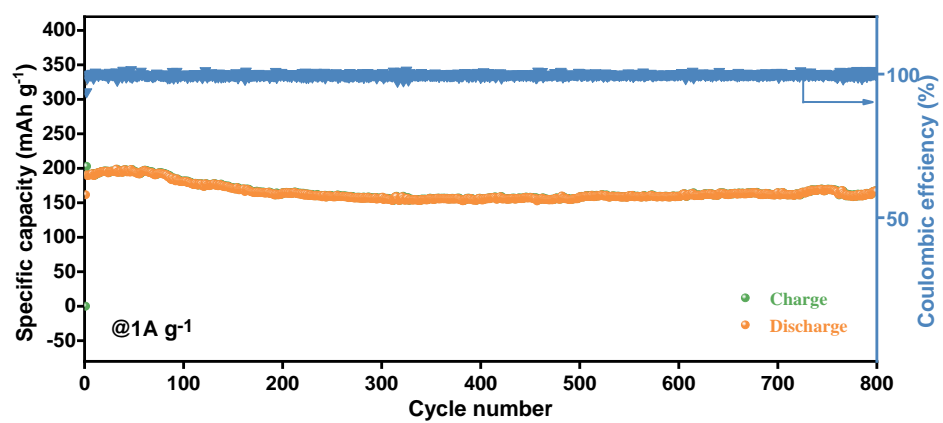
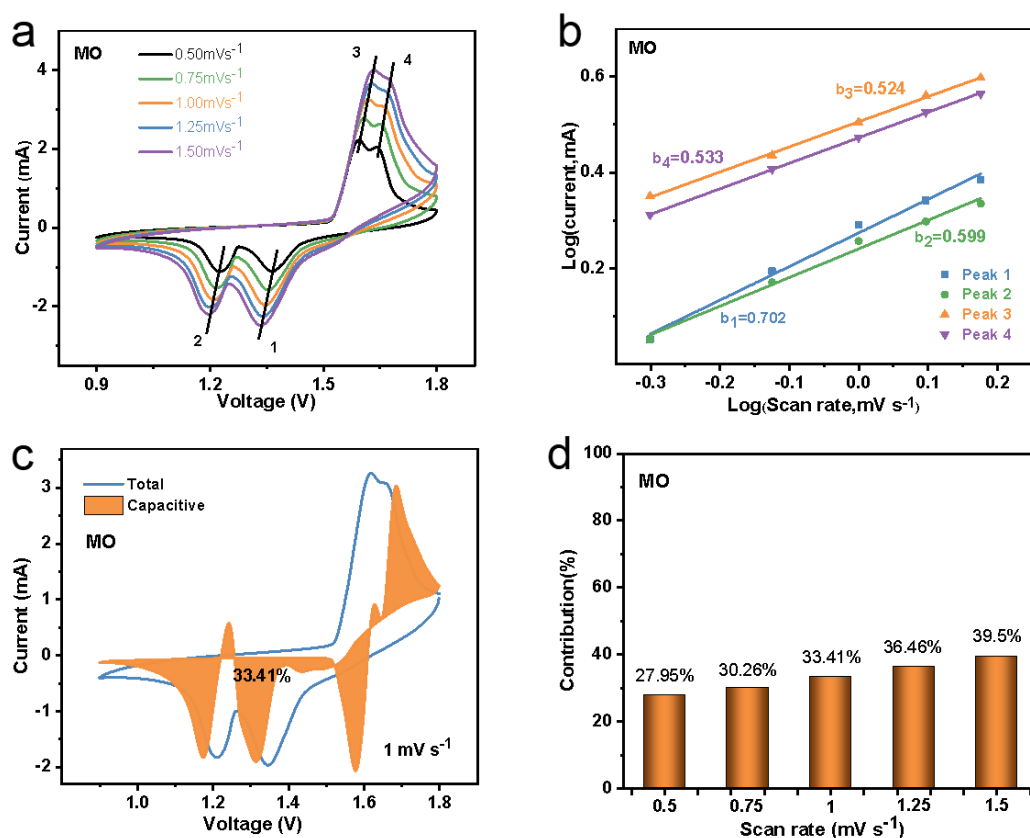**Figure S6**. Cycling performance and the corresponding coulombic efficiency of NFMO at 1.0A g^{-1}.

Figure S7. (c) CV curves of the MO electrode at various scan rates. (d) The corresponding plots of log (current) vs log (scan rate) of MO at each redox peak, and corresponding b values. (e) Capacitive and diffusion-controlled percentage of MO at a scan rate of 1 mV s^{-1}. (f) Contribution ratios of the capacitive capacities and diffusion-controlled capacities in the MO electrode.
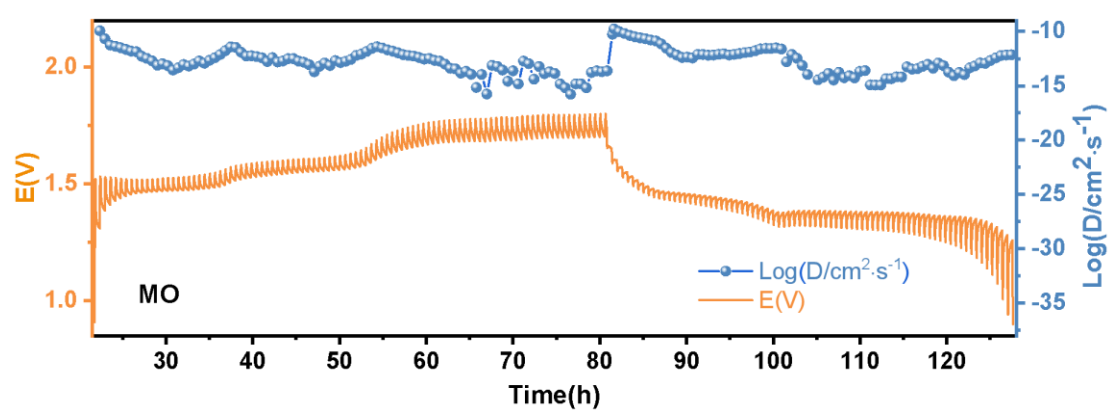
Figure S8. GITT curves and Diffusion coefficients calculated of MO at charge/discharge states.
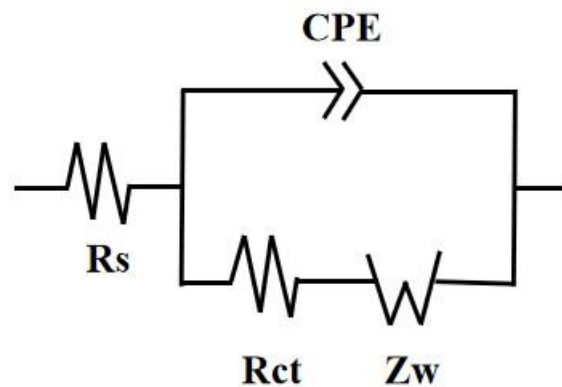
Figure S9. Equivalent circuit model.

The fitting results of EIS and equivalent circuit (EC) model are shown in Figure 4b and S9. The EC model is composed of three parts: Rct, Rs and Warburg impedance elements. The non-ideal capacitor Q and capacitor C are mutually connected in parallel, besides, C and Q are replaced by constant phase element (CPE) to simplify the model.
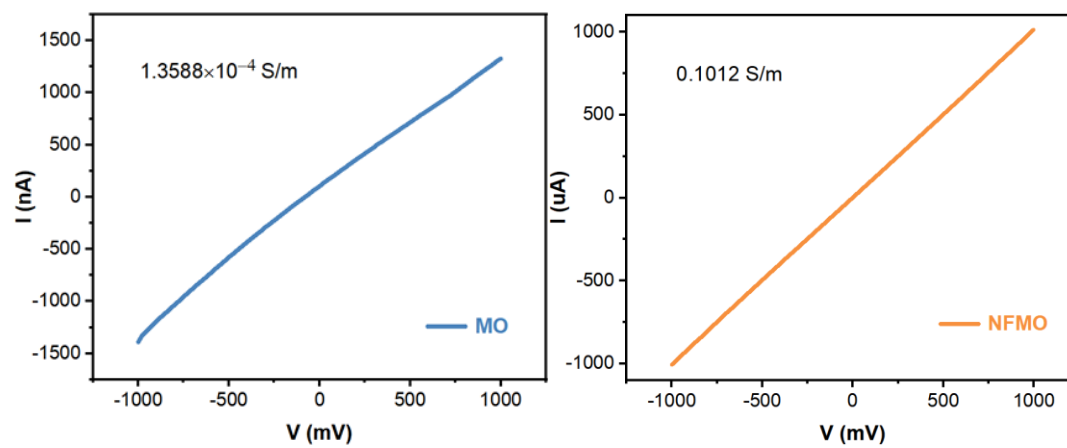
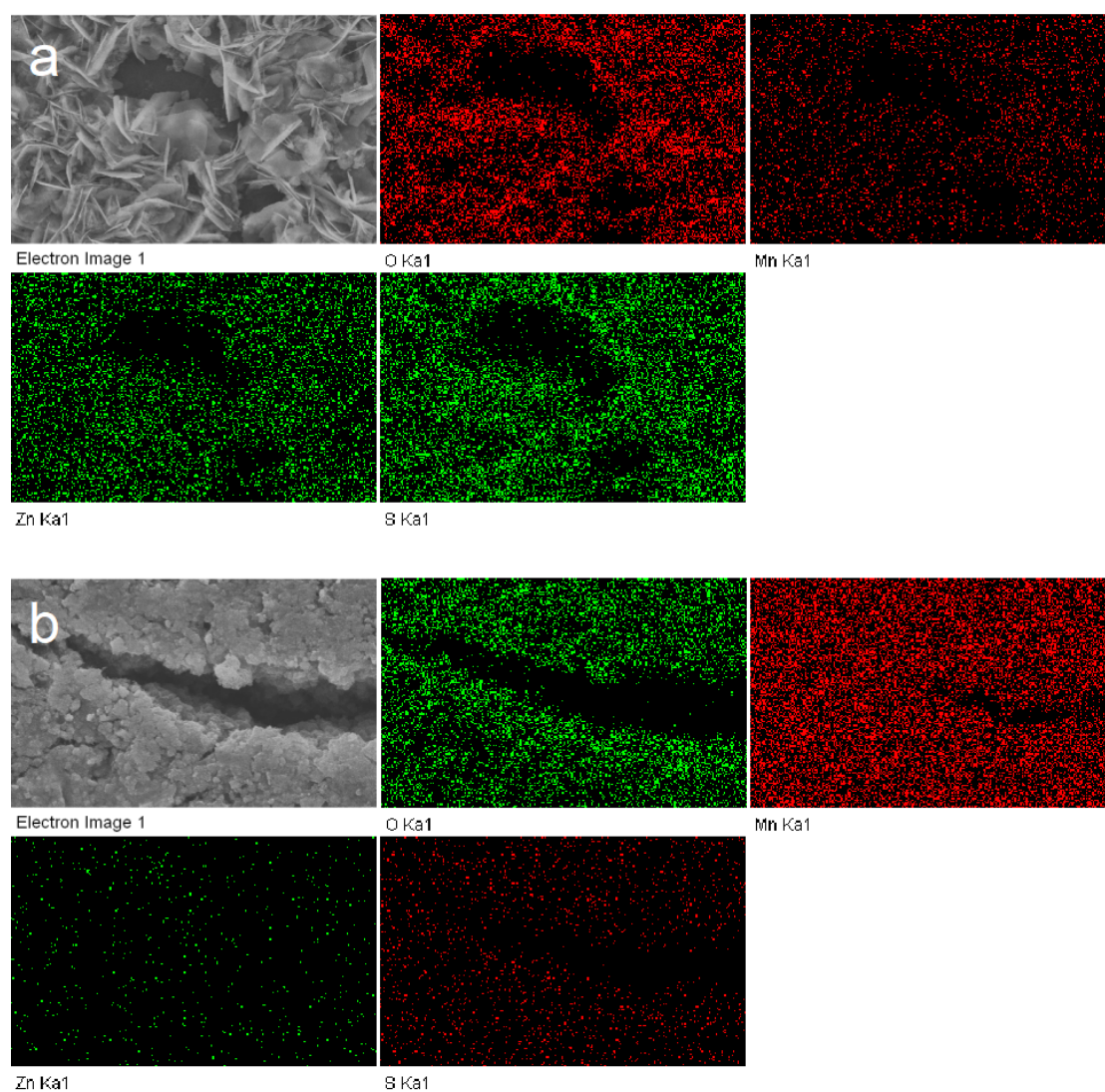**Figure S10**. Voltage-current curve of MO and NFMO.

Figure S11. (a) Images for SEM and elemental mapping images of NFMO discharged to 0.9 V in the first cycle. (b) Images for SEM and elemental mapping images of NFMO charged to 1.8 V in the first cycle.

Table S4. Comparison of cathode performance in aqueous ZIBs between this work and other recent reports.

Cathode	Electrolyte	Voltage window	Specific capacity/Cycling performance	Ref
Fe/α-MnO$_2$@PPy	2 M ZnSO$_4$ + 0.1 M MnSO$_4$	0.8-1.9 V	270 mA h g^{-1} (100 mA g^{-1})	[1]
Ni$_{0.052}$K$_{0.112}$MnO$_2$·0.136H$_2$O	3 M ZnSO$_4$ + 0.2 M MnSO$_4$	1-1.8 V	130 mA h g^{-1} (3080 mA g^{-1}; 10C)	[2]
Ag-doped MnO$_2$	2 M ZnSO$_4$ + 0.1 M MnSO$_4$	0.8–1.8 V	315 mA h g^{-1} (50 mA g^{-1}); 171 mA h g^{-1} (1 A g^{-1})	[3]
K$_{0.36}$H$_{0.26}$MnO$_2$·0.28H$_2$O	3 M ZnSO$_4$ + 0.2 M MnSO$_4$	1-1.8 V	329.8 mAh g^{-1} (0.1C); 100.1mAh g^{-1} (10C)	[4]
Cu-doped MnO$_2$	2 M ZnSO$_4$ + 0.1 M MnSO$_4$	1-1.8 V	320mAh g^{-1} (0.5C)	[5]
Mg$_{0.9}$Mn$_3$O$_7$·2.7H$_2$O	3 M ZnSO$_4$ + 0.1 M MnSO$_4$	0.85–1.85 V	312 mAh g^{-1} (0.2 A g^{-1});	[6]
NFMO	3 M ZnSO$_4$ + 0.2 M MnSO$_4$	0.9-1.8 V	382 mA h g^{-1} (100 mA g^{-1}); 181 mA h g^{-1} (3000 mA g^{-1})	This work

Reference

1. Xu, J.W.; Gao, Q.L.; Xia, Y.M.; Lin, X.S.; Liu, W.L.; Ren, M.M.; Kong, F.G.; Wang, S.J.; Lin, C. High-performance reversible aqueous zinc-ion battery based on iron-doped alpha-manganese dioxide coated by polypyrrole. *J. Colloid Interface Sci.* **2021**, *598*, 419-429, doi:10.1016/j.jcis.2021.04.057.

2. Zhao, Q.; Song, A.; Zhao, W.; Qin, R.; Ding, S.; Chen, X.; Song, Y.; Yang, L.; Lin, H.; Li, S., et al. Boosting the Energy Density of Aqueous Batteries via Facile Grotthuss Proton Transport. *Angew. Chem., Int. Ed.* **2021**, *60*, 4169-4174, doi:10.1002/anie.202011588.

3. Liao Y.; Yang C.; Xu Q.; Zhao W.; Zhao J.; Wang K.; Chen H. Ag-Doping Effect on MnO_2 Cathodes for Flexible Quasi-Solid-State Zinc-Ion Batteries. *Batteries* **2022**, *8*, 267, doi:10.3390/batteries8120267.

4. Ding, S.; Liu, L.; Qin, R.; Chen, X.; Song, A.; Li, J.; Li, S.; Zhao, Q.; Pan, F. Progressive "Layer to Hybrid Spinel/Layer" Phase Evolution with Proton and Zn^{2+} Co-intercalation to Enable High Performance of MnO2-Based Aqueous Batteries. *ACS Appl. Mater. Interfaces* **2021**, *13*, 22466-22474, doi:10.1021/acsami.1c03671.

5. Fenta, F.W.; Olbasa, B.W.; Tsai, M.-C.; Weret, M.A.; Zegeye, T.A.; Huang, C.-J.; Huang, W.-H.; Zeleke, T.S.; Sahalie, N.A.; Pao, C.-W., et al. Electrochemical transformation reaction of Cu–MnO in aqueous rechargeable zinc-ion batteries for high performance and long cycle life. *J. Mater. Chem. A* **2020**, *8*, 17595-17607, doi:10.1039/d0ta04175k.

6. Li, J.; Luo, N.; Kang, L.; Zhao, F.; Jiao, Y.; Macdonald, T.J.; Wang, M.; Parkin, I.P.; Shearing, P.R.; Brett, D.J.L., et al. Hydrogen-Bond Reinforced Superstructural Manganese Oxide As the Cathode for Ultra-Stable Aqueous Zinc Ion Batteries. *Adv. Energy Mater.* **2022**, 2201840, doi:10.1002/aenm.202201840.